TIGHTLY-COUPLED RTK/INS INTEGRATED NAVIGATION USING A LOW-COST GNSS RECEIVER AND A MEMS IMU

Xiao Sun[1] , Yuan Zhuang[1, 2,*], Shaohua Chen[1], Yuxin Shao[1], Dong Chen[1]

[1] State Key Laboratory of Information Engineering in Surveying, Mapping and Remote Sensing, Wuhan University, Wuhan 430079, China. (e-mail: xsun@whu.edu.cn (X. Sun))
[2] Wuhan Institute of Quantum Technology, Wuhan 430206, China.

Commission III, WG III/1

KEY WORDS: Integrated navigation, RTK, INS, Tightly coupled integration, GNSS-challenging environment.

ABSTRACT:

The Global Navigation Satellite System (GNSS) real-time kinematics (RTK) is a technology to provide centimeter-level navigation services in outdoor areas. GNSS/INS integration is a typical integrated navigation system, including loosely, tightly, and ultra-tightly coupled integration, which has been studied for decades. Although GNSS aiding INS is a relatively mature system, RTK is rarely used to be integrated with INS. In this work, we present a model with a tightly-coupled (TC) scheme to integrate RTK and INS using an extended Kalman Filter (EKF). Multi-GNSS multi-frequency double-differenced pseudo-ranges and carrier phases are the updates of the measurement model. To make the ambiguity resolution, we used the well-known LAMBDA algorithm to search for the possible ambiguity series, and then use the best integer equivariant (BIE) method to decide on the most likely ambiguities with a proper weighting strategy to select from the ambiguity candidates. To test the performance of the proposed TC integration model, we implemented two field vehicular tests with a low-cost GNSS module equipped with a Micro-Electro-Mechanical System (MEMS) IMU. Using this low-cost platform, our RTK/INS integrated navigation engine can achieve centimeter-level navigation solutions under open sky conditions. In harsh environments, our TC integration system navigates on two scenarios with mean errors of 0.48 and 0.57 m, which is 51% and 28% better than a loosely-coupled system.

1. INTRODUCTION

The Global Navigation Satellite System (GNSS) real-time kinematics (RTK) is a technology to provide centimeter-level positioning services in outdoor areas. Under open-sky conditions when ionosphere disturbances are not severe, RTK can achieve rapid or even instantaneous ambiguity resolution (AR) for short baseline. However, GNSS faces problems such as signal blockage and multipath in urban areas and other GNSS-challenging environments. To provide continuously reliable navigations, the inertial navigation system (INS) is considered as an ideal technology to aid GNSS. GNSS/INS integration is a typical integrated navigation system, including loosely, tightly, and ultra-tightly coupled integration, which has been studied for decades. Although GNSS aiding INS is a relatively mature system, most researches focused on single-frequency pseudo-range measurements, as a result, RTK is rarely used to be integrated with INS.

In the literature, a tightly-coupled RTK/INS integrated navigation system has been studied by a few works [Li et al., 2017, Yang et al., 2021, Li et al., 2019, Yan et al., 2021]. Reference [Li et al., 2017] discussed the integration of multi-GNSS single-frequency RTK and MEMS IMU. Further, the same group integrates RTK/INS with the aid of a monocular camera to use in GNSS-challenging environments [Li et al., 2019]. This work solved the problem in a harsh environment by using a camera and a navigation-grade IMU. Reference [Yang et al., 2021] proposed a non-holonomic robust and adaptive Kalman filter to improve the robustness of the RTK/INS integrated system. Reference [Yan et al., 2021] studied the in-motion alignment in RTK/INS system for autonomous driving. Similar to RTK/INS, a tightly-coupled PPP-RTK/INS integrated system under the complex urban environments is discussed in [Li et al., 2021]. However, multi-GNSS multi-frequency RTK/INS tightly-coupled integration has rarely been explored, nor has been the use of a low-cost GNSS receiver with a MEMS IMU.

In this work, we present a model with a tightly coupled scheme to integrate RTK and INS using an extended Kalman Filter (EKF). Dual-frequency double-differenced (DD) pseudo-ranges and carrier phases are used as measurements. To make the ambiguity resolution, we used the well-known LAMBDA algorithm [Teunissen, 1995] to search for the possible ambiguity series, and then use the best integer equivariant (BIE) method [Teunissen, 2003] to decide on the most likely ambiguities with a proper weighting strategy to select from the ambiguity candidates.

To test the performance of our tightly coupled integration model, we did several field vehicular tests within the campus of Wuhan University. The test platform is built on an AgileX SCOUT mini robot, with an Aceinna OpenRTK330LI GNSS module equipped with a Micro-Electro-Mechanical System (MEMS) IMU. Using this low-cost platform, our RTK/INS integrated navigation can achieve centimeter-level navigation solutions under open sky conditions, both for loosely coupled (LC) and tightly coupled (TC) schemes. As for sheltered conditions, LC RTK/INS will not give reliable positioning solutions. Correspondingly, TC RTK/INS integration will moderately help with computing the states and makes the navigation trajectory smoother. Experimental results show our TC RTK/INS integration gets better positioning results than LC schemes and is suitable for low-cost outdoor navigations.

*Corresponding author. E-mail: yuan.zhuang@whu.edu.cn (Y. Zhuang)

2. METHODOLOGY

2.1 Multi-GNSS Multi-frequency RTK Model

GNSS uses the pseudo-range and carrier phase measurements to locate a target. The former is a kind of distance measurement and is irrelevant to carrier frequency. However, when we use carrier phases for positioning, these measurements should be transformed into ranges using the corresponding wavelengths. RTK uses DD observation equations to eliminate the atmospheric delays, clock errors, satellite orbit errors, etc., which goes [Li et al., 2017, Yang et al., 2021]

$$\nabla\Delta P_{rb}^{ij} = \nabla\Delta\rho_{rb}^{ij} + \nabla\Delta\varepsilon_{P,rb}^{ij} \tag{1}$$

$$\lambda\nabla\Delta\varphi_{rb}^{ij} = \nabla\Delta\rho_{rb}^{ij} + \lambda\nabla\Delta N_{rb}^{ij} + \nabla\Delta\varepsilon_{\varphi,rb}^{ij} \tag{2}$$

where $\nabla\Delta()_{rb}^{ij}$ indicates the DD symbol between satellites i,j and receivers r,b. P and φ are the pseudo-range and the carrier phase. λ is the wavelength to transform phases into ranges. ρ is the distance between a satellite and a receiver. N is the phase ambiguity and ε is the measurement error including noises and multipath errors. Please note that these equations hold only for short baselines when ionosphere disturbance is not severe.

For multi-GNSS multi-frequency RTK, we need to divide the carrier phase observations into categories referring to the GNSS systems and carrier frequency bands. For instance, the carrier frequency of GPS L1 (1575.42MHz) differs from that of BDS B1 (1562.098MHz). As a result, if we difference two measurements of these two bands, the ambiguity becomes $\lambda^{L1}N^{L1} - \lambda^{B1}N^{B1}$, which can not be derived as an integer any more. To maintain the integer property of the phase ambiguity, all the DD observation equations are discussed among the category with the same frequency band.

In each frequency band where at least two satellites are observable, we select a reference satellite to do differencing. The reference satellite is chosen with the highest elevation and relatively higher signal-to-noise ratios (SNR). To resolve the ambiguity, we use the well-known LAMBDA algorithm [Teunissen, 1995] to decide on several groups of ambiguity candidates, and then use the BIE method [Teunissen, 2003] to average these candidates with properly designed weights

$$N = \frac{w_i N_i}{\sum_i^n w_i}, \text{where } w_i = e^{-\frac{s_i}{2}} - e^{-\frac{s_{max}}{2}} \tag{3}$$

In (3), N_i is the i^{th} ambiguity within n candidates, and s_i is its normalized uncertainty, whose value has a lower bound of 1. An ambiguity N is an integer, or in another way, a fixed one only when all the candidates averaged are integers. A fixed ambiguity is with relatively small variance, while a float one is with a variance calculated by

$$\sigma_{float,i}^2 = \frac{w_i(N - N_i)^2}{\sum_i^n w_i} \tag{4}$$

Since in this work RTK is integrated with a MEMS IMU, whose accuracy is not high, IMU does not aid the ambiguity resolution.

2.2 Tightly Coupled RTK/INS Integration Scheme

In our TC multi-GNSS multi-frequency RTK/INS integrated navigation system, we choose error states of 21 dimensions to form the state vector

$$\mathbf{x} = \begin{bmatrix}\delta\mathbf{r}^T & \delta\mathbf{v}^T & \boldsymbol{\psi}^T & \delta\mathbf{b}_g^T & \delta\mathbf{b}_a^T & \delta\mathbf{s}_g^T & \delta\mathbf{s}_a^T\end{bmatrix}^T \tag{5}$$

where $\delta\mathbf{r}$, $\delta\mathbf{v}$, and $\boldsymbol{\psi}$ are position errors, velocity errors, and attitude errors. $\mathbf{b}_g$ and $\mathbf{b}_a$ are gyro bias errors and accelerometer bias errors, $\mathbf{s}_g$ and $\mathbf{s}_a$ are gyro scale factor errors and accelerometer scale factor errors. All these vectors are in the navigation frame (North-East-Down, NED). For a MEMS IMU, the differential states are simply modeled with only some dominant error terms, hence, the first three vectors are modeled in (6). Bias and scale factor errors are modeled with white noises, since there seems to be no evident noise correlation.

$$\begin{bmatrix}\dot{\boldsymbol{\psi}}^n \\ \delta\dot{\mathbf{v}}^n \\ \delta\dot{\mathbf{r}}^n\end{bmatrix} = \begin{bmatrix}-\mathbf{C}_b^n\delta\boldsymbol{\omega}_{ib}^b - \boldsymbol{\omega}_{in}^n \times \boldsymbol{\psi}^n \\ \left(\mathbf{C}_b^n\mathbf{f}_{ib}^b\right) \times \boldsymbol{\psi}^n + \mathbf{C}_b^n\delta\mathbf{f}_{ib}^b - (2\boldsymbol{\omega}_{ie}^n + \boldsymbol{\omega}_{en}^n) \times \delta\mathbf{v}^n + \delta\mathbf{g}^n \\ \delta\mathbf{v}^n - \boldsymbol{\omega}_{en}^n \times \delta\mathbf{r}^n\end{bmatrix} \tag{6}$$

In (6), $\mathbf{C}_b^n$ is the direction cosine matrix to transform from b-frame (body frame) to n-frame (navigation frame). $\mathbf{f}_{ib}^b$ and $\boldsymbol{\omega}_{ib}^b$ are accelerometer and gyro outputs. $\boldsymbol{\omega}_{in}^n$ is the angular velocity from i-frame (inertial frame) to n-frame, which is projected on n-frame (similar marks can be explained as this). $\delta\mathbf{g}^n$, $\delta\boldsymbol{\omega}_{ib}^b$, and $\delta\mathbf{f}_{ib}^b$ are calculated as follows.

$$\delta\mathbf{g}^n = \frac{2\mathbf{g}^n}{R+h} \tag{7}$$

$$\delta\boldsymbol{\omega}_{ib}^b = \delta\mathbf{b}_g + diag(\boldsymbol{\omega}_{ib}^b)\delta\mathbf{s}_g \tag{8}$$

$$\delta\mathbf{f}_{ib}^b = \delta\mathbf{b}_a + diag(\mathbf{f}_{ib}^b)\delta\mathbf{s}_a \tag{9}$$

Using (6)-(9), we could make the 21×21 state transition matrix $\boldsymbol{\Phi}$ in the discrete-time domain for Kalman prediction. The state and covariance prediction of EKF are calculated by

$$\mathbf{x}_k^- = \boldsymbol{\Phi}\mathbf{x}_{k-1} \tag{10}$$

$$\mathbf{P}_k^- = \boldsymbol{\Phi}\mathbf{P}_{k-1}\boldsymbol{\Phi}^T + \mathbf{Q} \tag{11}$$

where $\mathbf{Q}$ is the covariance of noise.

In our model, we use DD pseudo-range and carrier phase measurements to update. In the measurement model, the innovation vector $\mathbf{z}_k$ is expressed by

$$\mathbf{z}_k = \begin{bmatrix}\nabla\Delta\hat{\boldsymbol{\rho}}_{\mathrm{INS}} - \nabla\Delta\mathbf{P}_{\mathrm{GNSS}} \\ \nabla\Delta\hat{\boldsymbol{\rho}}_{\mathrm{INS}} - \lambda\left(\nabla\Delta\boldsymbol{\varphi}_{\mathrm{GNSS}} - \nabla\Delta\mathbf{N}\right)\end{bmatrix} \tag{12}$$

where $\hat{\boldsymbol{\rho}}_{\mathrm{INS}}$ is the predicted distance calculated by satellite positions and predicted receiver positions. Considering the lever arm between the GNSS receiver and the INS center, a single INS-predicted DD distance $\nabla\Delta\hat{\rho}_{\mathrm{INS}}$ can be calculated by

$$\begin{aligned}\nabla\Delta\hat{\rho}_{\mathrm{INS}} = &\left|\mathbf{r}_r^i\right| - \left|\mathbf{r}_b^i\right| - \left(\left|\mathbf{r}_r^j\right| - \left|\mathbf{r}_b^j\right|\right) \\ &- (\mathbf{e}^i - \mathbf{e}^j) \cdot \mathbf{C}_n^e(\delta\mathbf{r}^n - \mathbf{C}_b^n\boldsymbol{\ell}^b)\end{aligned} \tag{13}$$

where $\boldsymbol{\ell}^b$ is the lever arm vector in b-frame, $\mathbf{e}^i$ and $\mathbf{e}^j$ are unit vectors of between the satellite i, j and the receiver in e-frame.

The design matrix is calculated using unit vectors and the lever

arm vector [Li et al., 2017]

$$\mathbf{H}_k = \begin{bmatrix} \mathbf{H}_\rho^* \mathbf{C}_n^e & \mathbf{0}_{n_\rho \times 3} & \mathbf{H}_\rho^* \mathbf{C}_n^e \left[\left(\mathbf{C}_b^n \boldsymbol{\ell}^b \right) \times \right] & \mathbf{0}_{n_\rho \times 12} \\ \mathbf{H}_\varphi^* \mathbf{C}_n^e & \mathbf{0}_{n_\varphi \times 3} & \mathbf{H}_\varphi^* \mathbf{C}_n^e \left[\left(\mathbf{C}_b^n \boldsymbol{\ell}^b \right) \times \right] & \mathbf{0}_{n_\varphi \times 12} \end{bmatrix} \tag{14}$$

where $\mathbf{H}_\rho^*$ and $\mathbf{H}_\varphi^*$ are used for pseudo-range and carrier phase measurements, respectively. $\mathbf{H}_\rho^*$ is a matrix with a dimension $n_\rho \times 3$ (n_ρ is the number of DD pseudo-range observations), $\mathbf{H}_\varphi^*$ is with a dimension $n_\varphi \times 3$. Each line of them is a vector $\left(-\mathbf{e}^i + \mathbf{e}^j\right)^T$, corresponding to the satellite pair and its carrier frequency.

In addition, the covariance matrix $\mathbf{R}$ of DD observations influenced navigation performance much. In our scheme, we make the $\mathbf{R}$ matrix based on SNR, elevations, and the ambiguity variance calculated by (4), to form the following equation.

$$\sigma^2 = \sigma_N^2 \times \frac{10^{-\frac{\mathrm{SNR}-40}{10}}}{(\sin e)^2} \tag{15}$$

where σ_N^2 is the ambiguity variance discussed in subsection 2.1, e is the elevation.

2.3 Overall Architecture

We use accelerometer leveling and a given heading for attitude alignment. The initial position is set with a single point positioning (SPP) result. In addition, to simplify the navigation preparation, we set the accelerometer bias with a zero vector and the gyro bias with mean values of gyro measurements during the static phase. The initial scale factors are also set with zero.

The overall architecture of this RTK/INS integration after the alignment phase is shown in figure 1. We use the network RTK via NTRIP protocol to collect observations from a virtual base station. After collecting rover and base station data, we select a reference satellite for each frequency band and double-difference the observations based on the selected reference satellites. Then, we use the LAMBDA algorithm and BIE method to solve the ambiguities. The solved ambiguities, together with double-differenced carrier phases and pseudo-ranges, are fused with the INS-predicted DD ranges to form the innovations for our Kalman filter using the equation (12). After the process of an EKF, the states are fed back to INS for revision. Position, velocity, and attitude error states are also used to update the navigation outputs.

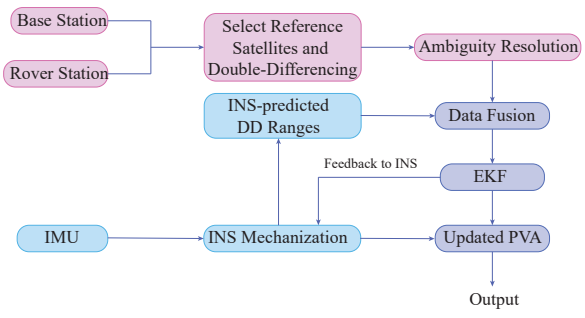

Figure 1: The system diagram of RTK/INS integration after the alignment phase.

3. EXPERIMENTAL SETUP

To test our TC RTK/INS integrated navigation system, we implemented several field vehicular tests within the campus of Wuhan University. The hardware platform is built on an AgileX SCOUT mini robot, with an Aceinna OpenRTK330LI GNSS module equipped with a Micro-Electro-Mechanical System (MEMS) IMU, which is shown in figure 2. The OpenRTK330LI GNSS module is of low-power consumption and can output the dual-frequency observations. The IMU model is OpenIMU330BI, whose performance parameters are listed in Table **??**. These parameters are read from its datasheet and are used to form the covariance matrix $\mathbf{Q}$ in (11).

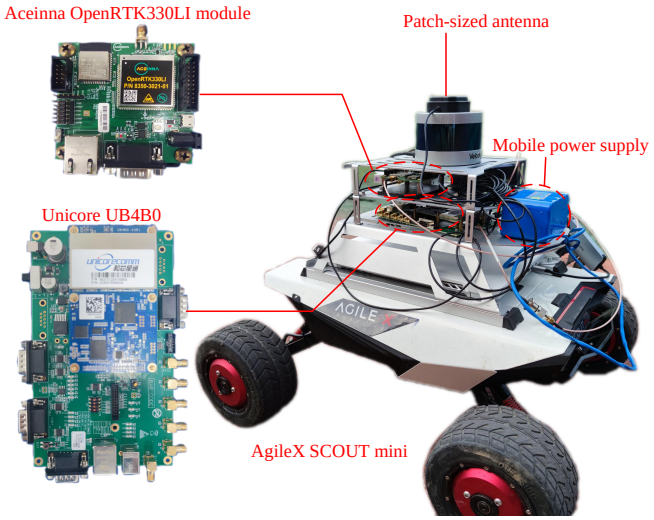

Figure 2: The hardware platform of our experiments.

We did two kinematic experiments using this system. In an open sky environment, it is easy for RTK to obtain a high proportion of fixed solutions. In this case, both LC and TC integration schemes can achieve accuracy within ten centimeters, and there are no significant differences between the results of these two schemes. To test the performance in harsh environments, we implemented two tests on sheltered roads. Figure 3 shows the trajectories of these two tracks. In these two tracks, most RTK solutions are float and may contain errors of several decimeters, or even larger than 1 meter. Some fixed solutions are wrongly fixed and contain errors greater than 1 decimeter.

Characteristics	Value
Sampling rate	100Hz
Velocity Random Walk	$6.67 \times 10^{-4} \mathrm{m/s}/\sqrt{\mathrm{s}}$
Angle Random Walk	$5.82 \times 10^{-5} \mathrm{rad}/\sqrt{\mathrm{s}}$
Bias Instability of Acce.	$1.96 \times 10^{-4} \mathrm{m/s^2}$
Bias Instability of Gyro	$7.27 \times 10^{-6} \mathrm{rad/s}$
Scale Factor Error of Acce.	0.4%
Scale Factor Error of Gyro	0.4%

Table 1: Technical characteristics of OpenIMU330BI from datasheet.

To evaluate the accuracy of our integrated navigation trajectories, we used a high-precision Unicore UB4B0 board (shown in figure 2), which adopts triple-frequency RTK technology. Since its power consumption is much higher than Aceinna OpenRTK330LI, a mobile power supply was installed to maintain the rated power of this Unicore board. In both two test sites, Unicore UB4B0 was capable of fixed solutions of a proportion higher than 99%, thus it was trustworthy to be regarded as a reference.

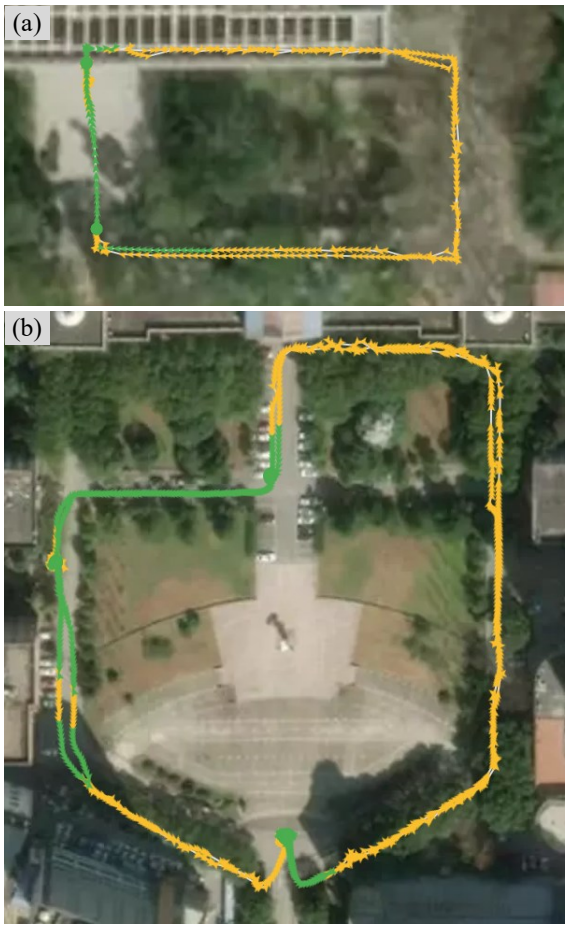

Figure 3: Two RTK tracks of our experimental results, on which the yellow parts are float solutions, green parts are fixed solutions. (a) Track 1 is a two-round clockwise loop on Sept. 26, 2021; (b) Track 2 is a two-round counterclockwise loop on Oct. 27, 2021.

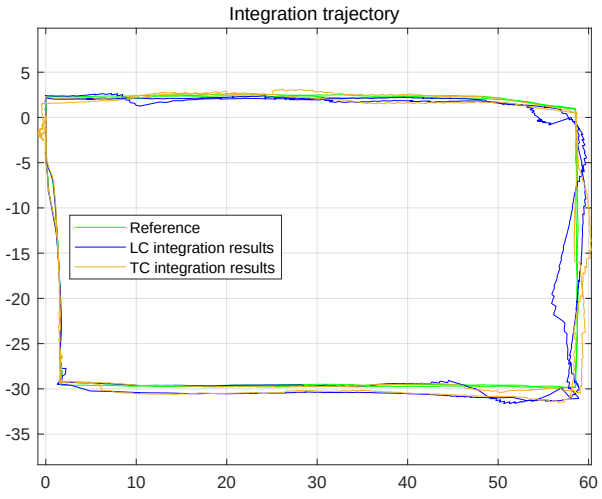

Figure 4: The integrated navigation results of track 1.

4. RESULTS AND ANALYSIS

In both track 1 and track 2, RTK measurements were 1 Hz, and the RTK/INS integrated navigation outputs were 10 Hz. Before the rover engine was started, it would stay static for a couple of minutes for alignment. In this alignment phase, no navigation results were computed. Thus, this phase is not shown in this section.

Track 1 is a two-round rectangular-like trajectory. The western part of this track was not sheltered much, in which RTK got a high proportion of fixed solution (shown in figure 3a). However, the rest scenarios of this track were severely sheltered, where the RTK accuracy declined to several decimeters or even meters. The observation condition (sheltered or not) matched well with our navigation results. Figure 4 shows that both LC and TC solutions in the eastern part are of worse accuracy than the western part. On sheltered conditions, the TC scheme got much better navigation performance than the LC scheme.

We used the Unicore UB4B0's RTK results as references to evaluate the errors. Figures 5 and 6 show positioning errors of track 1. In figure 5, there are many epochs where errors are evidently smaller. Those are static phases, which have been divided out. In figure 6a, the Cumulative Distribution Function (CDF) implies that the average error is centimeter-level. However, this is not practical. Figure 5 shows that a large proportion of the measurements were on the static points, and they are set on open-sky conditions. To truly present the error distribution, we excluded all the static points, and give the CDFs of only the kinematic phase. Figure 6b shows that a percentage of 67% TC positioning errors are within 0.63 m, compared with LC of 1.26 m. The largest error of TC is 2.73 m, compared with LC of 4.77 m.

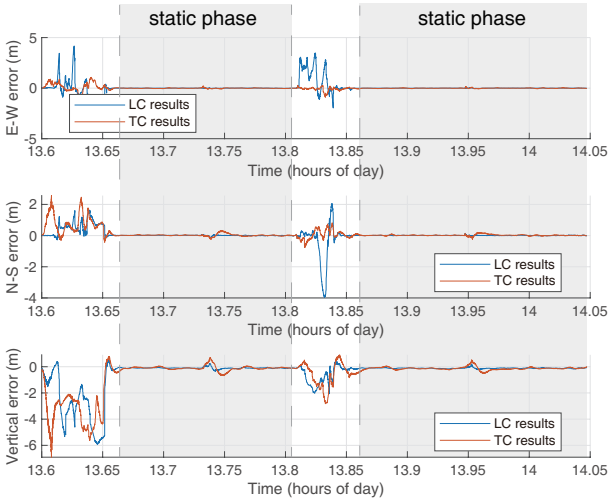

Figure 5: 3-dimensional error plots of track 1 in n-frame.

For track 2, we present results in a similar form with track 1. The positioning trajectory is shown in figure 7, and the error distributions are shown in figures 8 and 9. In the northeast part of figure 3, errors seem large and not continuous. Correspondingly, that part of figure 7 deviates much from the reference trajectory (green curve), especially the LC results. After excluding the static points, CDFs show that a percentage of 67% TC positioning errors are within 0.57 m, compared with LC of 1.00 m. The largest error of TC is 2.95 m, compared with LC of 10.10 m.

In conclusion, we made Table **??** to compare the error statistics of LC and TC integration results. Since we excluded the static

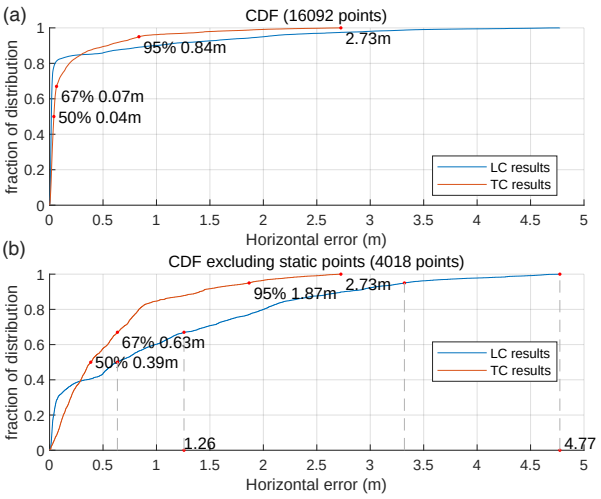

Figure 6: Track 1 CDFs of LC and TC integrated navigation results. (a) CDFs of all positioning results; (b) CDFs of only kinematic phase, static positioning points are excluded.

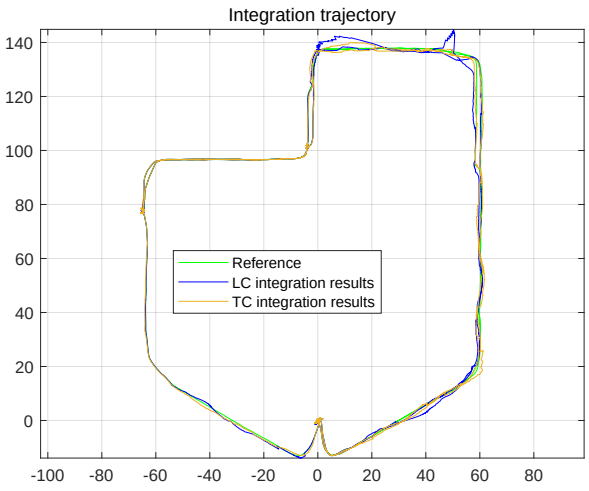

Figure 7: The integrated navigation results of track 2.

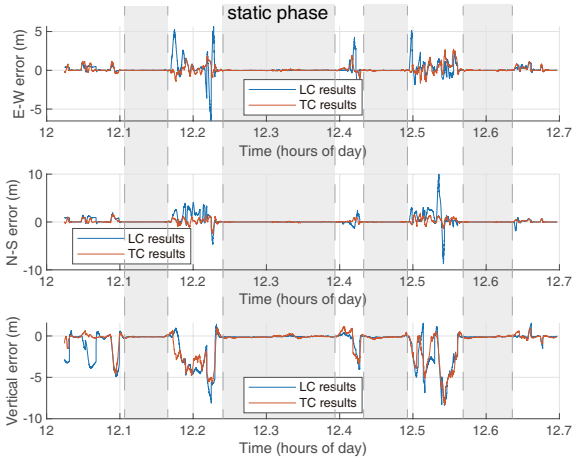

Figure 8: 3-dimensional error plots of track 2 in n-frame.

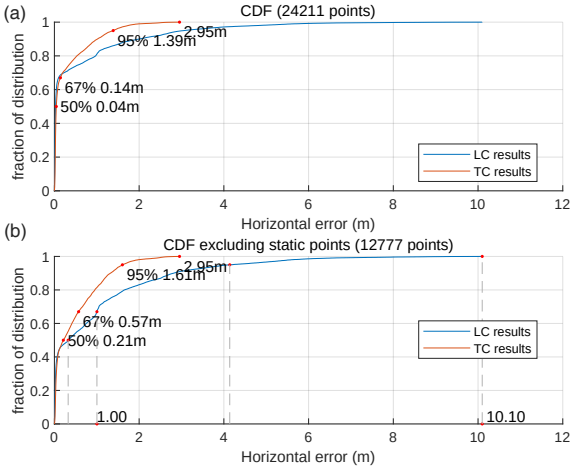

Figure 9: Track 2 CDFs of LC and TC integrated navigation results. (a) CDFs of all positioning results; (b) CDFs of only kinematic phase, static positioning points are excluded.

points, this table reflects the integrated navigation performances on sheltered conditions.

	Track 1		Track 2	
	LC	TC	LC	TC
50% error	0.63	**0.39**	0.32	**0.21**
67% error	1.26	**0.63**	1.00	**0.57**
95% error	3.32	**1.87**	4.14	**1.61**
100% error	4.77	**2.73**	10.10	**2.95**
mean error	0.79	**0.57**	0.98	**0.48**
RMS	1.53	**1.03**	1.76	**0.74**

Table 2: The error statistics of LC and TC navigation solutions in kinematic phases (Unit: m).

On sheltered conditions, TC integration results are much better than LC. The reasons are three folds: (1) Without external aids, a single low-cost RTK system can hardly give reliable positions on sheltered conditions. (2) In some epochs, solutions are even lost in the pure RTK (shown in figure 3a). In this case, the LC states may easily diverge since there are no updates in EKF. (3) Fixed solutions usually have small covariance and will give strong constraints to the Kalman system. Thus, some wrongly fixed solutions may mislead the LC integration system.

5. CONCLUSION

In this paper, we presented a multi-GNSS multi-frequency RTK/INS tightly-coupled integrated navigation model. Our RTK and INS TC models are comprehensively demonstrated. To verify its practical usage in GNSS-challenging environments, we did two tests on sheltered conditions using a low-cost GNSS receiver, a patch-sized antenna, and a MEMS IMU. When GNSS RTK is hard to give reliable solutions, TC RTK/INS can also output continuous positioning results with accuracy of several decimeters. In harsh environments, our TC integration system navigates on two scenarios with mean errors of 0.48 and 0.57 m, which is 51% and 28% better than an LC system.

ACKNOWLEDGEMENTS

This work was partly supported by Excellent Youth Foundation of Hubei Scientific Committee (2021CFA040) and Hubei Province InternationalScienceandTechnologyCollaboration Program (2021EHB012).

REFERENCES

Li, T., Zhang, H., Gao, Z., Niu, X. and El-sheimy, N., 2019. Tight fusion of a monocular camera, mems-imu, and single-frequency multi-gnss rtk for precise navigation in gnss-challenged environments. Remote Sensing.

Li, T., Zhang, H., Niu, X. and Gao, Z., 2017. Tightly-coupled integration of multi-gnss single-frequency rtk and mems-imu for enhanced positioning performance. Sensors.

Li, X., Li, X., Huang, J., Shen, Z., Wang, B., Yuan, Y. and Zhang, K., 2021. Improving ppprtk in urban environment by tightly coupled integration of gnss and ins. Journal of Geodesy 95(12), pp. 132.

Teunissen, P., 2003. Theory of integer equivariant estimation with application to gnss. Journal of Geodesy 77(7), pp. 402–410.

Teunissen, P. J. G., 1995. The least-squares ambiguity decorrelation adjustment: a method for fast gps integer ambiguity estimation. Journal of Geodesy 70(1), pp. 65–82.

Yan, Z., Zhang, C., Yang, Y. and Liang, J., 2021. A novel in-motion alignment method based on trajectory matching for autonomous vehicles. IEEE Transactions on Vehicular Technology 70(3), pp. 2231–2238.

Yang, Z., Li, Z., Liu, Z., Wang, C., Sun, Y. and Shao, K., 2021. Improved robust and adaptive filter based on non-holonomic constraints for RTK/INS integrated navigation. Measurement Science and Technology 32(10), pp. 105110.